Atomistic simulations of Mg vacancy segregation to dislocation cores in forsterite

Richard Skelton [a,b] and Andrew M. Walker[c,*]

[a] Research School of Earth Sciences, Australian National University, Canberra, ACT, 0200, Australia

(ORCID: 0000-0003-1583-2312)

[b] now at: Sandia National Laboratories, Livermore, CA 94550, USA

[c] School of Earth and Environment, University of Leeds, Leeds, LS2 9JT, UK

(ORCID: 0000-0003-3121-3255)

* Corresponding author: a.walker@leeds.ac.uk

This manuscript is a non-peer reviewed preprint submitted to EarthArXiv. It has been submitted to "Physics and Chemistry of Minerals" for consideration for publication.

Abstract

Interactions between dislocations in olivine and extrinsic cation vacancies created under hydrous or oxidizing conditions may influence the rheology of the Earth's upper mantle. In this study, we use atomic-scale simulations to calculate segregation energies for bare and protonated Mg vacancies to M1 and M2 sites in the core regions of [100](010) and [001](010) edge dislocations, and [100] and [001] screw dislocations. Calculated segregation energies are different for the two symmetry distinct M sites. The segregation energies calculated for the tightest binding M1 sites around [100] screw and [100](010) edge

dislocations are comparable to those calculated for the tightest binding M2 sites. Concentrations of M2 vacancy-related defects will thus be low in the core regions of these dislocations, given the comparatively high energy of these defects in the bulk lattice. In contrast, segregation energies for M2 defects to [001](010) edge dislocation cores are considerably lower than for equivalent M1 defects, and M2 vacancy concentrations around these dislocations will be similar to M1 vacancy concentrations. This means that the effect of magnesium vacancies on the mobility of the [001](010) edge dislocation may be significantly different to the effect on the mobility of the other dislocations considered.

Keywords: Forsterite, dislocation, point-defect segregation, atomistic simulation, cation vacancies

1. Introduction

Although nominally anhydrous, under the pressure and temperature conditions of the Earth's mantle, olivine can incorporate modest quantities of water into its crystal structure, primarily as protonated cation vacancies (e.g. Martin and Donnay, 1972; Bai and Kohlstedt, 1993; Kohlstedt et al., 1996). The water solubility limit in olivine is sensitive to the water and oxygen fugacities, and also increases with silica activity, consistent with incorporation via protonation of M site vacancies (Gaetani et al., 2014). Protonated vacancies interact with dislocations in the olivine crystal lattice, and may preferentially occupy atomic sites near such defects over sites in the bulk lattice, with the effect that vacancy-related defect concentrations are potentially much greater in the core region of a dislocation than in the unstrained bulk lattice. In extreme cases, impurity segregation can affect the bulk chemistry of minerals, as for example in the formation of striped chemical zoning in olivine during low strain-rate deformation, attributed to Fe^{2+} segregation to sub-grain boundaries formed by aligned arrays of edge dislocations (Ando et al., 2001). High-resolution synchrotron images show that the concentration of protonated defects in olivine is greatest around grain boundaries and cracks, demonstrating that these defects in

olivine will tend to segregate to locally strained regions of the crystal lattice (Sommer et al., 2008), while hydrogen concentrations near [001] dislocations in water-saturated olivine can be sufficiently great to induce climb dissociation of the dislocation core (Drury, 1991).

Interactions between point defects and dislocations can alter the mobility of the dislocation. Most commonly, dislocations experience solute drag when immobile impurities segregate to dislocation cores, pinning the dislocation in place and reducing strain rates accordingly (Cottrell and Bilby, 1949). However, some defects can increase dislocation mobility in the glide creep regime by reducing the Peierls barrier to glide, including vacancies in fcc Al (Lauzier et al., 1989; Lu and Kaxiras, 2002), hydrogen in Fe (Taketomi et al., 2008), or interstitial O defects in UO_2 (Ashbee and Yust, 1982; Keller et al., 1988). In olivine, interactions between water-related defects, occurring primarily as protonated vacancies may facilitate deformation by increasing dislocation mobility in the dislocation climb-controlled creep regime (e.g. Mackwell et al., 1985; Chen et al., 1998; Girard et al., 2013). Hydrous defects are thought to reduce the Peierls stress, σ_p, required for dislocation glide, whose measured value for hydrated olivine is ~1.6-2.9 GPa (Katayama and Karato, 2008), considerably lower than values measured for dry olivine polycrystals, which range from at least 3.8 GPa (Idrissi et al., 2016) to as much as ~15 GPa (Demouchy et al., 2013). Recent forced-oscillation measurements have suggested that Mg vacancies, produced to charge balance the oxidation of Fe^{2+} to Fe^{3+} (Stocker and Smyth, 1978; Nakamura and Schmalzried, 1983) may enhance attenuation in Fo_{90} olivine (Cline et al., 2018).. Natural dunites deforming in the dislocation creep regime also show a moderate sensitivity to the oxygen fugacity (Keefner et al., 2011). This suggests that bare cation vacancies may have a similar influence on the mechanical properties of olivine as protonated cation vacancies.

The short length scales characteristic of impurity segregation to dislocation cores mean that it can be difficult to study experimentally, although developments in the field of atom probe tomography mean that it is now possible to visualize impurity clouds around dislocation lines (Miller et al., 2006; Peterman et al., 2016). Theoretical modeling offers an alternative approach, allowing direct access to the atomic scale and control over system chemistry. While interactions between dislocations and point defects far from the dislocation line can be adequately modeled using linear elasticity theory, in the dislocation core non-elastic, atomic-scale relaxation can be substantial. One way to model a dislocation is to insert two or more dislocations into a 3D-periodic simulation cell, with their Burgers vectors **b** summing to zero to ensure continuity at the boundaries. Although this cell can be sufficiently small as to make the use of *ab initio* methods practical, care must be taken to minimize dislocation-dislocation interactions. An alternative is to embed a single dislocation in an isolated cluster of atoms with periodic boundary conditions along the dislocation line (Walker et al., 2005a). Both the cluster-based (Walker et al., 2005b) and supercell (Mahendran et al., 2017) approaches have been used to simulate [100] and [001] screw dislocations in forsterite, producing comparable dislocation core structures, although the latter study did not report core energies for either dislocation.

While atomistic modeling is a powerful tool for studying dislocations and their interactions with point defects, there are several limitations that restrict its range of applicability. Firstly, obtaining a converged dislocation core structure and energy may require the use of very large simulation cell, containing many hundreds or thousands of atoms, for which the computational cost of using quantum chemical methods such as DFT can be prohibitive. Instead, as in this study, interatomic potentials are more commonly used, which are parameterized by fitting to experimental data or *ab initio* calculations. The second problem is that the dislocation itself breaks the translational symmetry of the crystal, meaning that interactions between point defects cannot be parametrized using any of the techniques available for solid solutions,

such as cluster expansion (Sanchez et al., 1984) or Special Quasirandom Structures (Zunger et al., 1990), and the dislocation energy must be obtained from fully atomistic calculations. In practice, this limits calculations to the dilute limit.

In this study, we use the cluster-based approach to determine segregation energies for bare and protonated cation vacancies to dislocation cores in the forsterite (Mg_2SiO_4) end-member of the olivine solid solution. Since the silica activity in mantle peridodites is high, Mg vacancies are expected to be more abundant than Si vacancies. Consequently, we consider only Mg vacancies on the two symmetry distinct M sites, labeled M1 and M2. At low pressure, the easiest slip system in olivine is [100](010), but the [001](010) slip system becomes more active at high pressure (Couvy et al., 2004; Hilairet et al., 2012). Here, we use popular and well-tested empirical interatomic potential to calculate low energy core structures for the [100](010) and [001](010) edge and [100] and [001] screw dislocation. Segregation energies are calculated for bare and protonated M1 and M2 vacancies, written $\{V_{M1}\}''$, $\{2H_{M1}\}^X$, $\{V_{M2}\}''$ and $\{2H_{M2}\}^X$ in the Kröger-Vink notation (Kröger and Vink, 1956), to sites within the core regions of these dislocations. Energies for the different defects are compared to elucidate the effect of site occupation and hydrogen fugacity on the interaction between Mg vacancies to dislocations. In the bulk, M1 vacancies are energetically more favorable than M2 vacancies in the bulk lattice (Brodholt, 1997), but this may be different near dislocation cores, which may have implications for olivine rheology in dislocation-controlled creep regimes, as well as for Mg diffusion in crystals with high dislocation density.

2. Computational methods

Dislocation core structures and segregation energies were calculated using the cluster-based approach, in which an isolated dislocation is inserted at the axis of a 1D-periodic cylinder of atoms (Sinclair, 1971; Walker et al., 2005ab). The starting coordinates for the atoms are determined from the elastic

displacement field **u**(**r**) calculated using the sextic formulation for a dislocation in an anisotropic medium (Stroh, 1958). For edge dislocations, this is a non-conservative algorithm and atoms must be removed from the simulation cell to obtain a physically reasonable initial dislocation structure. To do this, a branch cut is created that is normal to both the Burgers and dislocation line vectors. Any atoms that are displaced across this branch cut by the displacement field **u**(**r**) are deleted. Atoms in close proximity to the branch cut are merged with any nearby atoms, if the distance between them falls below a specified threshold d_{min}. The cluster of atoms is subsequently divided into two concentric regions, with radii R_{I} and R_{II}. During the geometry optimization step, atoms in the inner region (region I) are permitted to relax freely, while those in the outer region (region II) are held fixed at the coordinates predicted using the elastic displacement field.

The total excess energy per unit length, E_{dis}, contained within radius r of an isolated dislocation is

$$E_{dis}(r) = E_{core} + \frac{Kb^2}{4\pi} log(r/r_c), \quad (1)$$

where K is the elastic energy coefficient and depends on the dislocation geometry and elastic constants C_{ij}, E_{core} is the energy contained within the core region (termed the core energy), and r_c is the radius of the dislocation core, within which the displacement field diverges from the predictions of linear elasticity. The core radius r_{c} is an undetermined parameter, whose value cannot determined from the radial excess energy of the dislocation. Its value must be chosen in order to set a gauge for the core energy. In this study, we use a core radius of $2b$, where b is the absolute magnitude of the Burgers vector.

The core energy is determined from atomistic cluster-based simulations by fitting equation (1) to the calculated radial dependence of the excess energy, which is the difference between the energy of a cluster containing the dislocation and a reference system containing an identical number of atoms. E_{core} is also

the excess energy of the dislocation at $r = r_c$. The excess energy is calculated from the energies of the individual atoms as

$$E_{excess}(r) = E_{dis}(r) - \sum_{species} n_{species}(r) E_{species}, \quad (2)$$

where $E_{dis}(r)$ is the total energy of the atoms within r of the dislocation line, the sum runs over the different atomic species present, $n_{species}(r)$ gives the number of atoms of each species within r, and $E_{species}$ is the energy of the species in the bulk lattice. This is equal to

$$E_{species} = 1/2 \left(E_{supercell} + E_{isolated} - E_{vac}\right), \quad (3)$$

where E_{vac} is the energy of a supercell from which one atom of the specified type has been removed, without relaxing the coordinates of the remaining atoms, $E_{supercell}$ is the energy of the supercell without a vacancy, and $E_{isolated}$ is the energy of an isolated atom of the specified type. In single-component crystals, this is identical to the energy of the unit cell divided by the number of atoms it contains.

The core energy and core displacement field of a dislocation in a two-region cluster depends on the radius of the relaxed region. A region I radius R_I = 25 Å was sufficient to guarantee convergence of the calculated core energies of the [100](010) edge and [100] and [001] screw dislocations to <10 meV/Å, while a larger region I with radius R_I = 35 Å was needed to achieve similar precision for the [001](010) edge dislocation. The coulomb energy was calculated using the Wolf summation (Wolf et al., 1999), which uses a charge neutralizing term to guarantee convergence of the energy at a finite distance. A cutoff range of r_{cut} = 15 Å and damping parameter ξ = 0.2 Å^{-1} were used, giving lattice parameters and elastic constants that differ from the values calculated using the Ewald method by <1%. As electrostatic interaction between ions is truncated at r_{cut}, the region II radius R_{II} of R_I+r_{cut} is used for all cluster calculations.

Due to the large size of the simulation cell, all calculations are performed using empirical interatomic potentials in the program GULP (Gale, 1997; Gale and Rohl, 2003). The interatomic potentials used are from the THB1 model, which was parameterized by fitting to experimental data (Sanders et al., 1984; Lewis and Catlow, 1985), and reproduces the physical properties of forsterite with reasonable accuracy (Price et al., 1987). Following Wright and Catlow (1994), we model protonated vacancies using the parameters developed by Schröder et al. (1992) to treat $(OH)^-$ groups in zeolite, incorporating the subsequent modifications made to the Morse potential by Gatzemeier and Wright (2006). This potential, labeled THB1, has been widely used to model point and extended defects in forsterite, including Mg point defects (Walker et al., 2009), surface structures and energetics (de Leeuw et al., 2000), and screw dislocation core structures and energies (Walker et al., 2005b).

In cluster calculations, the segregation energy E_{seg} of a single point defect at an atomic site in a dislocation core is determined by calculating the excess energy ΔE_{dis} of a point defect of the specified type embedded it in a simulation cell whose length is a multiple of the unit cell edge parallel to the dislocation line vector, $\boldsymbol{\xi}$, and comparing it with the excess energy ΔE_{perf} of an isolated defect in the bulk lattice, taken here to be the excess energy ΔE_{perf} of a point defect embedded in a 3D-periodic supercell of the material. This is equivalent to

$$E_{seg} = \left(E_{dfct+dis} - E_{dis}\right) - \left(E_{dfct+supercell} - E_{supercell}\right), \quad (4)$$

where E_{dis} is the energy of a cluster containing a dislocation, $E_{\text{dfct+dis}}$ is the energy of that same cluster with a single point defect inserted, $E_{\text{supercell}}$ is the energy of a defect-free 3D-periodic supercell, and $E_{\text{dfct+supercell}}$ is the energy of a supercell containing a point defect. Negative segregation energies indicate that the point defect will tend to bind to the dislocation to lower the total energy of the system, while positive segregation energies indicate the reverse.

$\{V_{M1}\}''$ and $\{V_{M2}\}''$ defects are inserted into a simulation by removing atoms of the specified type. As these defects are charged, a charge-neutralizing background was applied to the simulation cell, to maintain over charge neutrality. In addition to calculating segregation energies for bare Mg vacancies, segregation energies were also calculated for protonated Mg site vacancies. Constructing a $\{2H_{Mg}\}^X$ defect involves not only deletion of the Mg ion occupying the specified M site, and its replacement with two H ions, but also the replacement of two of the O ions around the site with oxygen ions using the hydroxyl potential. There are three symmetrically distinct O sites in olivine labeled O1, O2, and O3, leading a large number of possible configurations of the $\{2H_{M1}\}^X$ and $\{2H_{M2}\}^X$ defects. For both protonated defects, we use the configuration predicted by Walker et al. (2006) to have the lowest energy. In a protonated M1 vacancy, the hydrogen atoms are bonded to oxygen in the O2 site, while the hydrogen atoms in a protonated M2 vacancy are bonded to oxygen atoms on the O2 and O3 sites.

The segregation energies for the tightest binding site of the $\{V_{M1}\}''$, $\{V_{M2}\}''$, $\{2H_{M1}\}^X$, and $\{2H_{M2}\}^X$ defects for all four dislocations were converged to <0.05 eV by using supercells with length $n = 3$. The distance between a point defect and its closest periodic image is thus 17.960 Å for dislocations with line vector [001] and 14.346 Å for those with line vector [100]. Excess energies of isolated empty and protonated M-site vacancies were calculated using a simulation cell with dimensions 4*a*x2*b*x4*c*, where *a, b,* and *c* are the forsterite cell parameters, sufficiently large to guarantee convergence to within the tolerance specified for point defects in 1D-periodic clusters.

3. Dislocation core properties

The energy of a given dislocation depends on its coordinates within the crystallographic plane normal to $\boldsymbol{\xi}$. For each of the dislocations considered in this study, there are several possible symmetrically distinct origins (labeled in Fig. 1). In the case of edge dislocations, which also break any rotational symmetry of

192 the crystal about the line vector $\boldsymbol{\xi}$, the number of symmetrically distinct origins for a dislocation can be
193 even higher. Core energies for the most stable configuration found for each dislocation obtained by fitting
194 the computed radial variation of the excess energy (Fig. 3) to equation (1) are reported in Table 1. Also
195 shown are their associated elastic energy coefficients K, which are determined from the elastic constant
196 C_{ij} using the Stroh sextic theory (Stroh, 1958). The lowest energy core structures found are displayed in
197 Fig. 2.

198 [100] screw dislocations have higher core energies, E_{core}, than [001] screw dislocations. The calculated
199 core energies for the [100](010) and [001](010) edge dislocation slip systems are comparable. However,
200 the core radius r_c depends on the length of the Burgers vector, which is shorter for the [100](010) edge
201 dislocation, and E_{core} therefore corresponds to the energy of a smaller region. As can be seen in Table 1,
202 the [001] screw dislocation has the lowest core energy (1.50 eV/Å) and elastic energy coefficient (57.4
203 GPa) among the dislocations considered in this study. Consistent with these results, atomistic calculations
204 of generalized stacking fault energies have shown that both the relative volume change of SiO_4 tetrahedra
205 and the displacement of atoms away from the fault surface, which serve as measures of nonelastic strain,
206 are greater for [100](010) slip than [001](010) slip (Durinck et al., 2005). It follows that [100](010)
207 dislocations should be expected to have higher core energies than [001](010) dislocations.

208 Equilibrium core structures for the [100](010) and [001](010) edge dislocations are shown in Fig. 2ab.
209 As can be seen in Fig. 2a, the [100](010) edge dislocation has an asymmetric core structure, a
210 consequence of the absence of mirror planes parallel to [100]. The algorithm for creating an edge
211 dislocation creates something similar to a vacant M2 site near the [100](010) dislocation line. Inserting
212 an Mg atom at this site increases the core energy by 0.2 eV/Å. As a consequence, the [100](010) edge
213 dislocation has an empty channel parallel to $\boldsymbol{\xi}$, causing the oxygen ions closest to the dislocation line to

214 be under-coordinated. In contrast to the [100](010) edge dislocation, the stable core structure of the
215 [001](010) edge dislocation is symmetric, due to the existence of mirror planes parallel to (001) located
216 at z = 0.25 and z = 0.75, passing through the row of Si atoms parallel to [010]. Both edge dislocations
217 lie on the median planes of the $M2O_6$ polyhedra (y = 0.25/0.75). This is consistent with quantum
218 mechanical calculations of generalized stacking fault energies, which find that ideal shear stresses for
219 [100](010) and [001](010) slip are lowest when slip is localized at y = 0.25 (Durinck et al., 2005). The
220 Peierls stresses for dislocations gliding on (010) are similarly lowest when glide is on the plane at y =
221 0.25 (Durinck et al., 2007).

222 For the [100] screw dislocation, we find that the origin of the most stable core structure is (0.5, 0.25),
223 halfway between adjacent M2 sites (labeled site C in Fig. 1a), which has a calculated core energy of E_{core}
224 = 1.78 eV/Å. This core structure was also reported by Mahendran et al. (2017), who used the alternative
225 supercell approach. Earlier work using the cluster-based approach, by contrast, found that the dislocation
226 centered on the M1 site has a lower energy (Walker et al., 2005b), for which we compute a relatively
227 high core energy of 1.97 eV/Å. The discrepancy is likely due to the fact that Walker et al. (2005b)
228 searched for the minimum energy core structure using single point energy calculations at each possible
229 core position, whereas the core structures were relaxed in this study. Local atomic-scale structure thus
230 has a determining effect on the relative stability of the different core configurations for the [100] screw
231 dislocation in forsterite.

232 Whereas other dislocations gliding on (010) are located on the median plane of the sheet of $M2O_6$
233 octahedra, the most stable core structure of the [001] screw dislocation is centered on the column of
234 $M1O_6$ polyhedra running parallel to [001] (labeled site D in Fig. 1b), consistent with previous theoretical
235 calculations (Walker et al., 2005b; Mahendran et al., 2017). As found in previous studies (Carrez et al.,
236 2008), the [001] screw dislocation has a non-planar core. This is can be seen clearly in the sub-periodic

modulation of the displacement **u** of M1 sites located in the lattice plane a distance 1/2*b* above and below the glide plane. These atoms are displaced normal to the (010) glide plane, with the sense of this displacement alternating along [001] (see Fig. 2d). The SiO_4 tetrahedra in this plane undergo significant rotation, with the sign of this rotation alternating in the fashion as the sign of the displacement of neighboring M1 sites. This modulation causes the two-fold rotation center at z = 0.5, where *z* is the coordinate along the dislocation line, to disappear. In what follows, the region in which 0.0 <= *z* < 0.5 is referred to as the "lower" region, and the region with *z* satisfying 0.5 <= z < 1.0 as the "upper" region. In this labeling scheme, the lower region corresponds to those M1 sites that relax away from the (010) glide plane, and the upper region to the sites that relax toward it.

4. Segregation of Mg vacancies to dislocations

4.1 Excess energies of defects in the bulk lattice

Segregation energies are calculated from equation (4), which requires the excess energy of a point defect in the bulk lattice. This excess energy is defined as the difference between the energies of forsterite supercells of the same size, with and without a point defect. The excess energy of an $\{V_{M1}\}''$ defect, corrected for the interactions between charged defects, is 24.0 eV, while a $\{V_{M2}\}''$ defect has a modestly higher excess energy of 25.9 eV, reflecting the lower energy of a magnesium ion in M2 site. Similarly, the excess energy of a $\{2H_{M2}\}^X$ defect in the bulk lattice is 41.8 eV, significantly greater than the 39.4 eV excess energy calculated for the $\{2H_{M1}\}^X$ defect.

Creating an M1 vacancy, whether protonated or bare, is thus more energetically favorable than creating an M2 vacancy. $\Delta H_{M1\rightarrow M2}$, the enthalpy required to exchange an Mg vacancy between the M1 and M2 sub-lattices is 1.9 eV, identical to previous values of $\Delta H_{M1\rightarrow M2}$ calculated using empirical potentials

(Jaoul et al., 1995; Walker et al., 2009), but higher than the 0.81 eV energy difference predicted by DFT calculations (Brodholt, 1997). The energy difference $\Delta H_{M1\rightarrow M2}$ between the $\{2H_{M1}\}^X$ and $\{2H_{M2}\}^X$ defects, at 2.4 eV, is even greater than that for bare vacancies. As the relative concentrations of vacancies on the two sites depends exponentially on $\Delta H_{M1\rightarrow M2}$, M1 vacancies, whether bare or protonated, will be considerably more abundant than similar M2 vacancy-related defects in the bulk lattice.

4.2 Segregation of M1 vacancies

The segregation energy for the $\{V_{M1}\}''$ defect around a [100](010) edge dislocation is lowest for the three sites located directly below the dislocation line (Fig. 4a). The $\{V_{M1}\}''$ defect binds particularly tightly to the site directly below the glide plane, which has a segregation energy of -3.00 eV. Segregation energies for the $\{2H_{M1}\}^X$ defect are similarly lowest for the three sites immediately below the glide plane, although their segregation energies are more similar in value. E_{seg} = -2.30 eV for the site directly below the glide plane. For both defects, segregation energies decrease rapidly with distance from the dislocation line.

Segregation energies for M1 defects around [001](010) edge dislocations are shown in Fig. 5. $\{V_{M1}\}''$ defects bind to the sites immediately above the glide plane of [001](010) edge dislocations, with segregation energy -1.74 eV. As was found for $\{V_{M1}\}''$ around the [100](010) edge dislocation, segregation energies increase markedly away from the most stable binding site; the next lowest energy is -1.05 eV, corresponding to the M1 sites on either side of the tightest binding sites. As was found for [100](010) dislocations, $\{2H_{M1}\}^X$ defects segregating to [001](010) edge dislocations preferentially bind to sites directly below the glide plane and close to the dislocation line, albeit with considerably higher segregation energies than found for [100](010) edge dislocations. For the tightest binding site, which is located directly below the glide plane and on either side of the dislocation line, E_{seg} = -1.08 eV, and segregation energies are only marginally higher for M1 sites above the glide plane.

The calculated minimum segregation energies for M1 vacancies binding to screw dislocation cores are higher than those for the edge dislocations, consistent with the lower stresses induced by a screw dislocation. For the [100] screw dislocation, the low energy sites are distributed radially around the dislocation core (Fig. 6), with the tightest binding sites being those closest to the (010) glide plane. The tightest binding sites for the $\{V_{M1}\}''$ defect, at $\mathbf{r} \approx \pm[(1/2)\mathbf{c}+(1/4)\mathbf{b}]$ (**b** in this context referring to the unit cell length rather than the Burgers vector), have E_{seg} = -0.87 eV, while E_{seg} = -0.81 eV for the next most tightly bound sites, which are located at $\mathbf{r} \approx \pm[(1/2)\mathbf{c}-(1/4)\mathbf{b}]$. However, the sites closest to the dislocation line have comparatively high segregation energies (-0.20 eV). Comparing Fig. 6a and Fig. 6b, it can be readily seen that $\{2H_{M1}\}^X$ defects show greater site selectivity than $\{V_{M1}\}''$ defects, as the segregation energies for the sites at $\mathbf{r} \approx \pm[(1/2)\mathbf{c}-(1/4)\mathbf{b}]$, -0.99 eV, are considerably lower than those computed for any other site, while those at $\mathbf{r} \approx \pm[(1/2)\mathbf{c}+(1/4)\mathbf{b}]$ have considerably higher energies (-0.35 eV), comparable to the -0.40 eV of the M1 sites closest to the dislocation line. Segregation energies for $\{2H_{M1}\}^X$ defects decrease more rapidly with distance from dislocation line than do segregation energies calculated for bare M1 vacancies.

Segregation energies for defects around the [001] screw dislocation (Fig. 7) depend not only on their location in the plane normal to the line vector $\boldsymbol{\xi}$, but also on their position along the $\boldsymbol{\xi}$, due to the modulation of the crystal structure along the dislocation line. For the bare M1 vacancy the lowest segregation energy site is -0.77 eV within the lower region, compared with -0.61 eV in the upper region. Segregation energies for the $\{2H_{M1}\}^X$ defect are more sensitive to location along the dislocation line. E_{seg} = -0.89 eV for the tightest binding site in the lower region, while the lowest segregation energy found for any site in the upper region is only -0.62 eV. For both bare and protonated defects, E_{seg} is generally lower for sites in the lower region, and E_{seg} can be positive for sites in the upper region, particularly the site through which the dislocation line passes. Defect concentrations will be lower in this region than in

303 the bulk lattice. Segregation energies for M1 vacancy-related defects in the upper and lower regions of
304 the [001] screw dislocation are anti-correlated, which may inhibit pipe diffusion along this dislocation as
305 vacancy migration entails successive jumps between high and low segregation energy sites.

306 *4.3 Segregation of M2 vacancies*

307 The lowest segregation energy site for $\{V_{M2}\}''$ around the [100](010) edge dislocation is not at the glide
308 plane, but at x = 0 on the first sheet of $M2O_6$ octahedra below the dislocation (Fig. 4). The segregation
309 energy of the most stable binding site (-3.93 eV) is considerably lower than that calculated at any other
310 location in the dislocation core, matching the behavior found for $\{V_{M1}\}''$ defects segregating to this
311 dislocation. The energies of the next tightest binding sites, those immediately adjacent to the dislocation
312 on the glide plane, are considerably higher, with E_{seg} = -1.4 eV. As was found for the M1 defects
313 segregating to this dislocation, the segregation energy surface of the $\{2H_{M2}\}^X$ defect is profoundly
314 different to that of the $\{V_{M2}\}''$ defect. Unlike $\{V_{M2}\}''$, $\{2H_{M2}\}^X$ binds to sites near the glide plane, with
315 the lowest energies found for the four sites closest to the dislocation line. The two sites closest to the
316 dislocation line, which are above the glide plane, have E_{seg} = -1.53 eV, while E_{seg} =
317 -1.82 eV for the two sites below the glide plane. Above the glide plane, segregation energies rapidly
318 decay to zero.

319 The tightest binding sites for $\{V_{M2}\}''$ defects segregating to [001](010) edge dislocations are in the sheet
320 of $M2O_6$ octahedra above the glide plane (Fig. 5). For these sites, the segregation energy is -3.64 eV.
321 The M2 site closest to the dislocation line has the next lowest energy, with E_{seg} = -3.40 eV. The
322 segregation energy for $\{2H_{M2}\}^X$ defects is lowest for the site at x = 0 is the sheet of $M2O_6$ octahedra
323 below the glide plane, for which E_{seg} = -3.07 eV. Unlike $\{V_{M2}\}''$ defects, segregation of $\{2H_{M2}\}^X$ defects

to the M2 site closest to the dislocation line is comparatively unfavorable, with E_{seg} = -0.70 eV for this site.

The low energy sites for $\{V_{M2}\}''$ and $\{2H_{M2}\}^X$ defects around the [100] screw dislocation are distributed radially around the dislocation line (Fig. 6). However, for both defects the tightest binding sites are located near the (010) glide plane. The energy for segregation of $\{V_{M2}\}''$ defects to the sites closest to the dislocation line is -1.74 eV. The lowest segregation energies correspond to the next closest sites to the dislocation line, for which E_{seg} = -1.91 eV. For protonated M2 vacancies, the sites immediately adjacent to the dislocation line have the lowest energy, with E_{seg} = -2.46 eV. Segregation energies for protonated vacancies increase more markedly with distance from the dislocation line than for bare M2 vacancies, and E_{seg} is only -1.39 eV for the next tightest binding site.

As was found for defects on the M1 sub-lattice around [001] screw dislocations, M2 segregation energies vary along the dislocation line (Fig. 7). The sites for which the segregation energy of $\{V_{M2}\}''$ is a minimum are found in the lower region. For these sites, E_{seg} = -1.89 eV, whereas the lowest segregation energy for any site in the upper region is -1.06 eV. At upper mantle temperatures, the concentration of $\{V_{M2}\}''$ defects will therefore be orders magnitude greater in the lower region than the upper region, due to the exponential variation of relative concentrations on ΔH. For $\{2H_{M2}\}^X$ defects, the six sites closest to the closest to the dislocation line have nearly identical segregation energies (approximately -1.73 eV). In contrast to $\{V_{M2}\}''$ defects, the minimum energies in each region are comparable, and $\{2H_{M2}\}^X$ bind as strongly to sites in the upper region as they do to sites in the lower region.

5. Discussion

5.1 Comparing segregation energies for M1 and M2 defects

For all dislocations considered in this study, $\{V_{M2}\}''$ defects bind more tightly to core sites than $\{V_{M1}\}''$ defects. The difference between the minimum segregation energies for the two defects around a [100](010) edge dislocation is 0.93 eV. Comparable values of 1.04 and 1.18 eV are found for the [100] and [001] screw dislocations, respectively. Except in the case of [100](010) edge dislocations, for which the minimum segregation energy for the $\{2H_{M2}\}^X$ defect is 0.48 eV higher than that for the $\{2H_{M1}\}^X$ defect, $\{2H_{M2}\}^X$ defects bind more strongly to dislocation cores, relative to the equivalent defect in the unstrained lattice, than $\{2H_{M1}\}^X$ defects. M2 vacancy-related defects will be more strongly concentrated near dislocation cores, relative to the bulk, than M1 defects. However, the lower absolute energies of M1 vacancies mean that these defects will remain more abundant near dislocation cores than M2 vacancies. The ratio of defect concentrations on the two sites, $[\{V_{M1}\}'']/[\{V_{M2}\}'']$ will nevertheless still be lower near a dislocation than in the bulk lattice, as will the ratio $[\{2H_{M1}\}^X]/[\{2H_{M2}\}^X]$, except around [100](010) edge dislocations.

However, while this means that the concentration of M2 vacancies, relative to M1 vacancies, is greater in the vicinity of a dislocation core than in the bulk, this does not necessarily imply that they are lower energy. Indeed, only in the case of [001](010) edge dislocations are the differences between the lowest segregation energies of the $\{V_{M1}\}''$ and $\{V_{M2}\}''$ defects comparable to $\Delta H_{M1\rightarrow M2}$ for the bulk lattice. The energy difference for protonated M1 and M2 vacancies is lower than the bulk $\Delta H_{M1\rightarrow M2}$ for all four dislocations, so that creation of a protonated M1 vacancy near the dislocation core is still more favorable than creation of a protonated M2 vacancy. Assuming that vacancy-related defects can lubricate glide of dislocations in olivine, it is probable that the effect will vary with the distance of the vacant site from the glide plane. In forsterite, this implies that M2 vacancies will have a greater lubrication effect for dislocations gliding on (010) than M1 vacancies, as glide occurs primarily on the (010)-parallel sheet of $M2O_6$ octahedra. However, as shown here, with the exception of the [001](010) edge dislocation, M2

368 vacancies are much less abundant than M1 vacancies near dislocation cores, which could limit the
369 magnitude of the glide lubrication effect.

370 The [001](010) edge dislocation represents a partial exception, as $\{V_{M2}\}''$ defects bind particularly
371 strongly to the core sites of this dislocations. The segregation energy (relative to an equivalent defect in
372 the bulk) of the tightest binding site for $\{V_{M2}\}''$ defects in the core region of this dislocation is 1.9 eV
373 lower than that of the tightest binding M1 site, comparable to the value of $\Delta H_{M1\rightarrow M2}$ in the bulk lattice
374 environment. This means that absolute energies for the $\{V_{M1}\}''$ and $\{V_{M2}\}''$ defects segregating to tightest
375 binding sites in [001](010) edge dislocation cores are identical, and their concentrations close the
376 dislocation line will be similar. The low energy of the tightest binding M2 vacancy for this defect is
377 readily explained by the fact that the dislocation runs through an M2 site, so that the region of highest
378 strain coincides with an M2 site. The difference between the minimum segregation energies for $\{2H_{M2}\}^X$
379 and $\{2H_{M1}\}^X$ defects around a [001](010) edge dislocation core is 2.0 eV. This is 0.4 eV lower than the
380 energy difference between the two defects in the absence of strain field. Consequently, although hydrated
381 M1 vacancies will be more abundant than M2 vacancies in the dislocation core, the relative abundance
382 of the latter will be far greater near the core of [001](010) edge dislocations than in the bulk lattice.

383 *5.2 Segregation energies of bare versus protonated defects*

384 Among dislocations in forsterite gliding on (010), segregation energies are lower for edge than screw
385 dislocations and, in general, lower for dislocations with Burgers vector **b** = [100] than those with **b** =
386 [001]. Considering only the sites with the lowest segregation energies, bare and protonated M1 and M2
387 vacancies should be more abundant near [100](010) than [001](010) edge dislocations, and with
388 generally higher concentrations for [100] screw dislocations than [001] screw dislocations. The spatial
389 distribution of segregation energies for protonated and bare M site vacancies for a specific dislocation

are similar. However, as noted in the previous section, the fine details of the segregation energy surfaces can vary considerably and non-trivially between $\{V_{M1}\}''$ and $\{2H_{M1}\}^X$, and $\{V_{M2}\}''$and $\{2H_{M2}\}^X$. In this section, we will attempt to quantify the degree to which protonation changes segregation energies.

The degree to which the segregation energies for two defects around a particular dislocation are similar to one another can be quantified by computing a similarity measure for the segregation energy surfaces around the dislocation core. One such measure is the cosine similarity measure, which is computed for two vectors $\mathbf{x}_1$ and $\mathbf{x}_2$ as

$$s_{12}(x_1, x_2) = x_1 \cdot x_2 / (\|x_1\| \|x_2\|), \quad (5)$$

The similarity s_{12} = -1 when the vectors are anti-correlated, while s_{12} = 1 for perfectly correlated vectors. The cosine similarity measure is widely used in data mining to compare data sets, with applications ranging from facial verification (e.g. Nguyen and Bai, 2010), to comparing linguistic data sets (e.g. Liao and Xu, 2015), and automated text classification (e.g. Song et al., 2009). Here, we represent a segregation energy surface for a single point defect around a dislocation as a vector of length equal to the number of sites, whose entries correspond to the segregation energies of each site. Thus bare and protonated vacancies around the same dislocation can be compared provided that segregation energies have been computed for the same list of sites, as is the case in this study. However, the similarity measure cannot be straightforwardly compared between slip systems, as the list of sites will be different. Computed values of s_{12} for the M1 and M2 sites within 15 Å of the dislocation line are given in Table 3.

The similarity s_{12} of the M2 sub-lattice is strictly positive for all dislocations, meaning that the segregation energies of $\{V_{M2}\}''$ and $\{2H_{M2}\}^X$ defects to dislocations in forsterite are invariably positively correlated. For all four dislocations considered in this study, the cosine similarity measure is positive, indicating a broad correlation between segregation energies of bare and protonated vacancies on the same

412 sub-lattice. Bare and protonated Mg vacancies around [100](010) edge dislocations have relatively
413 similar energies for both sub-lattices and, and s_{12}(M1) is only ~3% greater than the corresponding value
414 for the M2 sub-lattice. Around [001](010) edge dislocations, s_{12} differs considerably for defects on the
415 two sub-lattices around [001](010) edge dislocations, with s_{12}(M1)/s_{12}(M2) = 1.20. In contrast, the
416 similarity measures computed using the calculated segregation energy surfaces for screw dislocations are
417 considerably greater on the M2 sub-lattice, with s_{12}(M2)/s_{12}(M1) = 1.14 for [100] screw dislocations and
418 1.19 for [001] screw dislocation.

419 The [001] screw dislocation has a modulated core structure, and defects on M1 sites that are adjacent
420 along [001] have different segregation energies, as can be seen in Fig. 7. Considering the segregation
421 energies for the M1 sites at $y = 0.0$ (Fig. 7ab) and $y = 0.5$ (Fig. 7cd) separately, we find similarities s_{12} =
422 0.889 and s_{12} = 0.44. Thus, although $\{V_{M1}\}''$ and $\{2H_{M1}\}^X$ segregation energies are more strongly
423 correlated for the M1 sites which displace away from the (010) glide plane, they are only weakly
424 correlated for the M1 sites that are displaced towards the glide plane. As can be seen in Fig. 7, the pattern
425 of segregation energies for the M2 vacancies similarly varies between the upper and lower regions of the
426 [001] screw dislocation. However, the similarity measure varies much less between the two regions for
427 M2 vacancies than M1 vacancies, with $s_{12} = 0.87$ for sites in the lower region, and $s_{12} = 0.94$ in the upper
428 region.

429 *5.3 Defect segregation and olivine deformation*

430 Vacancy-lubrication of dislocation glide has been reported in a range of different materials. Generalized
431 stacking fault energy (GSFE) parametrized Peierls-Nabarro calculations have suggested that interstitial
432 H may facilitate dislocation glide in Al meta (Lu et al. 2001), while the presence of interstitial O in hyper-
433 stoichiometric UO_2 (i.e. UO_{2+x}, $x > 0$) is known to reduce the critical resolved shear stress (Keller et al.

1988), an effect attributed to interactions between the interstitial impurities and the dislocation core (Ashbee and Yust, 1982). One possible explanation is that interactions between the dislocation core and an adsorbed vacancy defect reduce the Peierls stress, although the precise mechanism remains unclear. Deformation experiments in the glide-controlled creep regime show that the critical resolved shear stress decreases from 3.8-15.0 GPa in dry olivine (Idrissi et al., 2016; Demouchy et al., 2013) to 1.6-2.9 GPa for olivine under water-saturated conditions (Katayama and Karato, 2008). This CRSS represents the stress required for deformation at 0 K, and is referred to by Katayama and Karato as the Peierls stress, although it actually represents a weighted average of the Peierls stresses for several active slip systems.

The solubility limit of vacancy-related defects in the olivine crystal lattice is relatively high, and can reach nearly 0.9 % for protonated vacancies at 12 GPa pressure (Smyth et al., 2006). However, these concentrations are probably not sufficiently great to create Peierls stress reductions of the magnitude reported by Katayama and Karato (2008). However, the strongly negative segregation energies calculated for both edge and screw dislocations mean that the concentration of vacancy-related defects will be many times greater in the dislocation core than in the bulk crystal lattice. It follows that the influence of vacancy-related defects on the deformation of olivine in dislocation-controlled creep regimes can be significant, even at low bulk concentrations. Moreover, $\{V_{M2}\}''$ and $\{2H_{M2}\}^X$ defects were found to have considerably lower segregation energies than equivalent defects on the M1 sub-lattice, and the relative abundance of M2 defects will be much higher in dislocation cores than in the bulk lattice. This is significant, as M2 vacancies are expected to have the greatest influence on the Peierls stress for dislocations gliding on (010), as these dislocations glide on the median plane of the sheet of $M2O_6$ octahedra.

6. Conclusions

Vacancy related defects are important for understanding the material properties of olivine. The addition of small quantities of water to Fo_{90} olivine deforming in the glide creep regime increases strain rates, indicating a reduction of the Peierls stress. This has been plausibly attributed to lubrication of dislocation glide by protonated cation vacancies interacting with the dislocation, a process similar to the vacancy lubrication phenomenon invoked to explain flow stress variations for a range of materials. Concentrations of protonated vacancies or similar vacancy-related defects present at the dislocation core need to be high for the lubrication effect to be substantial. However, H concentration in mantle olivine is typically low, with <1000 ppm H/Si, although water contents may reach higher values in the deep upper mantle. Ferric iron, an important source of bare vacancies in silicate minerals, has a similarly low abundance, except in the most oxidized regions of the mantle (Kelley and Cottrell, 2009). Consequently, vacancy lubrication is possible only if vacancy related defects bind strongly to sites around dislocation cores.

In this study, we have used cluster-based computational simulations to compute segregation energies for both bare and protonated Mg vacancies around dislocations in forsterite. These segregation energies can be < -1.0 eV, suggesting that vacancy-related defect concentrations near the dislocation core may be orders of magnitude higher than in the bulk lattice, especially at low to moderate temperature. These are precisely the temperature conditions at which dislocation glide is most important for the deformation of olivine. However, not all vacancies are equal and, while the energy of an $\{V_{M2}\}''$ or $\{2H_{M2}\}^X$ defect is considerably lower near an edge or screw dislocation line than an equivalent defect in the bulk lattice, Mg vacancies still preferentially occupy M1 sites near dislocations, as they do in the bulk lattice. Thus, even though concentrations of vacancy related defects at the dislocation core may be high, they may occupy sites whose ability to directly influence dislocation glide is limited. The easy glide plane for dislocations gliding on (010) is the median plane of the sheet of $M2O_6$ octahedra, and M2 vacancies located this glide plane may play a critical role in lubricating dislocation glide. Such strategically located

vacancies are expected to be most abundant around [001](010) edge dislocations, and any increase in the glide mobility is likely to be most significant for the [001](010) slip system.

Acknowledgements

AMW is grateful for support from the UK Natural Environment Research Council (NE/K008803/1 and NE/M000044/1). RS is supported by an Australian Government Research Training Program (RTP) Scholarship. Calculations were performed on the Terrawulf cluster, a computational facility supported through the AuScope initiative. AuScope Ltd is funded under the National Collaborative Research Infrastructure Strategy (NCRIS), an Australian Commonwealth Government Programme. This work used the ARCHER UK National Supercomputing Service (http://www.archer.ac.uk). Ian Jackson is thanked for his helpful comments.

References

Ando J, Shibata Y, Okajima Y, et al (2001) Striped iron zoning of olivine induced by dislocation creep in deformed peridotites. Nature 414:893–895. doi: 10.1038/414893a

Ashbee KHG, Yust CS (1982) A mechanism for the ease of slip in UO2+x. Journal of Nuclear Materials 110:246–250. doi: 10.1016/0022-3115(82)90152-0

Bai Q, Kohlstedt DL (1993) Effects of chemical environment on the solubility and incorporation mechanism for hydrogen in olivine. Phys Chem Minerals 19:460–471. doi: 10.1007/BF00203186

Brodholt J (1997) Ab initio calculations on point defects in forsterite (Mg2SiO4) and implications for diffusion and creep. American Mineralogist 82:1049–1053. doi: 10.2138/am-1997-11-1201

Carrez P, Walker AM, Metsue A, Cordier P (2008) Evidence from numerical modelling for 3D spreading of [001] screw dislocations in Mg2SiO4 forsterite. Philosophical Magazine 88:2477–2485. doi: 10.1080/14786430802363804

Chen J, Inoue T, Weidner DJ, et al (1998) Strength and water weakening of mantle minerals, olivine, wadsleyite and ringwoodite. Geophys Res Lett 25:575–578. doi: 10.1029/98GL00043

Cline II CJ, Faul UH, David EC, et al (2018) Redox-influenced seismic properties of upper-mantle olivine. Nature 555:355–358. doi: 10.1038/nature25764

Cottrell AH, Bilby BA (1949) Dislocation Theory of Yielding and Strain Ageing of Iron. Proc Phys Soc A 62:49. doi: 10.1088/0370-1298/62/1/308

Couvy H, Frost DJ, Heidelbach F, et al (2004) Shear deformation experiments of forsterite at 11 GPa - 1400°C in the multianvil apparatus. European Journal of Mineralogy 16:877–889. doi: 10.1127/0935-1221/2004/0016-0877

Demouchy S, Tommasi A, Boffa Ballaran T, Cordier P (2013) Low strength of Earth's uppermost mantle inferred from tri-axial deformation experiments on dry olivine crystals. Physics of the Earth and Planetary Interiors 220:37–49. doi: 10.1016/j.pepi.2013.04.008

Drury MR (1991) Hydration-induced climb dissociation of dislocations in naturally deformed mantle olivine. Phys Chem Minerals 18:106–116. doi: 10.1007/BF00216603

Durinck J, Legris A, Cordier P (2005) Pressure sensitivity of olivine slip systems: first-principle calculations of generalised stacking faults. Phys Chem Minerals 32:646–654. doi: 10.1007/s00269-005-0041-2

Durinck J, Carrez P, Cordier P (2007) Application of the Peierls-Nabarro model to dislocations in forsterite. European Journal of Mineralogy 19:631–639. doi: 10.1127/0935-1221/2007/0019-1757

Gaetani GA, O'Leary JA, Koga KT, et al (2014) Hydration of mantle olivine under variable water and oxygen fugacity conditions. Contrib Mineral Petrol 167:965. doi: 10.1007/s00410-014-0965-y

Gale JD (1997) GULP: A computer program for the symmetry-adapted simulation of solids. J Chem Soc, Faraday Trans 93:629–637. doi: 10.1039/A606455H

Gale JD, Rohl AL (2003) The General Utility Lattice Program (GULP). Molecular Simulation 29:291–341. doi: 10.1080/0892702031000104887

Gatzemeier A, Wright K (2006) Computer modelling of hydrogen defects in the clinopyroxenes diopside and jadeite. Phys Chem Minerals 33:115–125. doi: 10.1007/s00269-006-0059-0

Girard J, Chen J, Raterron P, Holyoke CW (2013) Hydrolytic weakening of olivine at mantle pressure: Evidence of [1 0 0](0 1 0) slip system softening from single-crystal deformation experiments. Physics of the Earth and Planetary Interiors 216:12–20. doi: 10.1016/j.pepi.2012.10.009

Hilairet N, Wang Y, Sanehira T, et al (2012) Deformation of olivine under mantle conditions: An in situ high-pressure, high-temperature study using monochromatic synchrotron radiation. J Geophys Res 117:B01203. doi: 10.1029/2011JB008498

Idrissi H, Bollinger C, Boioli F, et al (2016) Low-temperature plasticity of olivine revisited with in situ TEM nanomechanical testing. Science Advances 2:e1501671. doi: 10.1126/sciadv.1501671

Jaoul O, Bertran-Alvarez Y, Liebermann RC, Price GD (1995) Fe□Mg interdiffusion in olivine up to 9 GPa at T = 600–900°C; experimental data and comparison with defect calculations. Physics of the Earth and Planetary Interiors 89:199–218. doi: 10.1016/0031-9201(94)03008-7

Katayama I, Karato S (2008) Low-temperature, high-stress deformation of olivine under water-saturated conditions. Physics of the Earth and Planetary Interiors 168:125–133. doi: 10.1016/j.pepi.2008.05.019

Keefner JW, Mackwell SJ, Kohlstedt DL, Heidelbach F (2011) Dependence of dislocation creep of dunite on oxygen fugacity: Implications for viscosity variations in Earth's mantle. J Geophys Res 116:B05201. doi: 10.1029/2010JB007748

Keller RJ, Mitchell TE, Heuer AH (1988) Plastic deformation in nonstoichiometric UO2+x single crystals—I. Deformation at low temperatures. Acta Metallurgica 36:1061–1071. doi: 10.1016/0001-6160(88)90160-5

Kelley KA, Cottrell E (2009) Water and the Oxidation State of Subduction Zone Magmas. Science 325:605–607. doi: 10.1126/science.1174156

Kohlstedt DL, Keppler H, Rubie DC (1996) Solubility of water in the α, β and γ phases of (Mg,Fe)2SiO4. Contrib Mineral Petrol 123:345–357. doi: 10.1007/s004100050161

Kröger FA, Vink HJ (1956) Relations between the Concentrations of Imperfections in Crystalline Solids. Solid State Physics 3:307–435. doi: 10.1016/S0081-1947(08)60135-6

Lauzier J, Hillairet J, Vieux-Champagne A, Benoit W (1989) The vacancies, lubrication agents of dislocation motion in aluminium. J Phys: Condens Matter 1:9273. doi: 10.1088/0953-8984/1/47/001

Leeuw NH de, Parker SC, Catlow CRA, Price GD (2000) Modelling the effect of water on the surface structure and stability of forsterite. Phys Chem Min 27:332–341. doi: 10.1007/s002690050262

Lewis GV, Catlow CRA (1985) Potential models for ionic oxides. J Phys C: Solid State Phys 18:1149. doi: 10.1088/0022-3719/18/6/010

Liao H, Xu Z (2015) Approaches to manage hesitant fuzzy linguistic information based on the cosine distance and similarity measures for HFLTSs and their application in qualitative decision making. Expert Systems with Applications 42:5328–5336. doi: 10.1016/j.eswa.2015.02.017

Lu G, Zhang Q, Kioussis N, Kaxiras E (2001) Hydrogen-Enhanced Local Plasticity in Aluminum: An Ab Initio Study. Phys Rev Lett 87:095501. doi: 10.1103/PhysRevLett.87.095501

Lu G, Kaxiras E (2002) Can Vacancies Lubricate Dislocation Motion in Aluminum? Phys Rev Lett 89:105501. doi: 10.1103/PhysRevLett.89.105501

Mackwell SJ, Kohlstedt DL, Paterson MS (1985) The role of water in the deformation of olivine single crystals. J Geophys Res 90:11319–11333. doi: 10.1029/JB090iB13p11319

570 Mahendran S, Carrez P, Groh S, Cordier P (2017) Dislocation modelling in Mg 2 SiO 4 forsterite: an
571 atomic-scale study based on the THB1 potential. Modelling Simul Mater Sci Eng 25:054002. doi:
572 10.1088/1361-651X/aa6efa
573 Martin RF, Donnay G (1972) Hydroxyl in the mantle. American Mineralogist 57:554–570
574 Miller MK (2006) Atom probe tomography characterization of solute segregation to dislocations and
575 interfaces. J Mater Sci 41:7808–7813. doi: 10.1007/s10853-006-0518-5
576 Nakamura A, Schmalzried H (1983) On the nonstoichiometry and point defects of olivine. Phys Chem
577 Minerals 10:27–37. doi: 10.1007/BF01204323
578 Nguyen HV, Bai L (2010) Cosine Similarity Metric Learning for Face Verification. In: Computer
579 Vision – ACCV 2010. Springer, Berlin, Heidelberg, pp 709–720
580 Peterman EM, Reddy SM, Saxey DW, et al (2016) Nanogeochronology of discordant zircon measured
581 by atom probe microscopy of Pb-enriched dislocation loops. Science Advances 2:e1601318. doi:
582 10.1126/sciadv.1601318
583 Price GD, Parker SC, Leslie M (1987) The lattice dynamics and thermodynamics of the Mg2SiO4
584 polymorphs. Phys Chem Minerals 15:181–190. doi: 10.1007/BF00308782
585 Sanchez JM, Ducastelle F, Gratias D (1984) Generalized cluster description of multicomponent
586 systems. Physica A: Statistical Mechanics and its Applications 128:334–350. doi: 10.1016/0378-
587 4371(84)90096-7
588 Sanders MJ, Leslie M, Catlow CRA (1984) Interatomic potentials for SiO2. J Chem Soc, Chem
589 Commun 1271–1273. doi: 10.1039/C39840001271
590 Schröder K-P, Sauer J, Leslie M, et al (1992) Bridging hydrodyl groups in zeolitic catalysts: a
591 computer simulation of their structure, vibrational properties and acidity in protonated faujasites (H□Y
592 zeolites). Chemical Physics Letters 188:320–325. doi: 10.1016/0009-2614(92)90030-Q
593 Sinclair JE (1971) Improved Atomistic Model of a bcc Dislocation Core. Journal of Applied Physics
594 42:5321–5329. doi: 10.1063/1.1659943
595 Smyth JR, Frost DJ, Nestola F, et al (2006) Olivine hydration in the deep upper mantle: Effects of
596 temperature and silica activity. Geophys Res Lett 33:L15301. doi: 10.1029/2006GL026194
597 Sommer H, Regenauer-Lieb K, Gasharova B, Siret D (2008) Grain boundaries: a possible water
598 reservoir in the Earth's mantle? Miner Petrol 94:1–8. doi: 10.1007/s00710-008-0002-9
599 Song W, Li CH, Park SC (2009) Genetic algorithm for text clustering using ontology and evaluating
600 the validity of various semantic similarity measures. Expert Systems with Applications 36:9095–9104.
601 doi: 10.1016/j.eswa.2008.12.046
602 Stocker RL, Smyth DM (1978) Effect of enstatite activity and oxygen partial pressure on the point-
603 defect chemistry of olivine. Physics of the Earth and Planetary Interiors 16:145–156. doi:
604 10.1016/0031-9201(78)90085-7

605 Stroh AN (1958) Dislocations and Cracks in Anisotropic Elasticity. Philosophical Magazine 3:625–
606 646. doi: 10.1080/14786435808565804
607 Taketomi S, Matsumoto R, Miyazaki N (2008) Atomistic simulation of the effects of hydrogen on the
608 mobility of edge dislocation in alpha iron. J Mater Sci 43:1166–1169. doi: 10.1007/s10853-007-2364-5
609 Walker AM, Gale JD, Slater B, Wright K (2005a) Atomic scale modelling of the cores of dislocations
610 in complex materials part 1: methodology. Phys Chem Chem Phys 7:3227–3234. doi:
611 10.1039/B505612H
612 Walker AM, Gale JD, Slater B, Wright K (2005b) Atomic scale modelling of the cores of dislocations
613 in complex materials part 2: applications. Phys Chem Chem Phys 7:3235–3242. doi:
614 10.1039/B505716G
615 Walker AM, Demouchy S, Wright K (2006) Computer modelling of the energies and vibrational
616 properties of hydroxyl groups in α- and β-Mg2SiO4. European Journal of Mineralogy 18:529–543. doi:
617 10.1127/0935-1221/2006/0018-0529
618 Walker AM, Woodley SM, Slater B, Wright K (2009) A computational study of magnesium point
619 defects and diffusion in forsterite. Physics of the Earth and Planetary Interiors 172:20–27. doi:
620 10.1016/j.pepi.2008.04.001
621 Wright K, Catlow CRA (1994) A computer simulation study of (OH) defects in olivine. Phys Chem
622 Minerals 20:515–518. doi: 10.1007/BF00203222
623 Zunger A, Wei S-H, Ferreira LG, Bernard JE (1990) Special quasirandom structures. Phys Rev Lett
624 65:353–356. doi: 10.1103/PhysRevLett.65.353
625

Tables

Table 1 Calculated core energies and elastic energy coefficients and core energies for the most stable configurations of dislocations in forsterite

	E_{core} (eV/Å)	K (GPa)
[100](010) edge dislocation	2.42±0.04	135.0
[001](010) edge dislocation	2.46±0.07	92.3
[100] screw dislocation	1.78±0.02	79.1
[001] screw dislocation	1.50±0.03	57.4

Table 2 Minimum segregation energies (in eV) for defects around dislocations in forsterite. In each of these cases, the minimum energy site is close to the dislocation core, where atomic-scale effects dominate over elastic terms such the size-effect and inhomogeneity interactions

	[100](010) edge dislocation	[100] screw dislocation	[001](010) edge dislocation	[001] screw dislocation
$\{V_{M1}\}''$	-3.00	-0.87	-1.74	-0.76
$\{2H_{M1}\}^X$	-2.30	-1.00	-1.08	-0.89
$\{V_{M2}\}''$	-3.93	-1.91	-3.64	-1.89
$\{2H_{M2}\}^X$	-1.82	-2.46	-3.07	-1.73

Table 3 Values of the cosine similarity measure for bare and protonated M sites around the various dislocations in forsterite

	[100](010) edge dislocation	[100] screw dislocation	[001](010) edge dislocation	[001] screw dislocation
M1	0.89	0.78	0.81	0.73
M2	0.86	0.89	0.68	0.87

638 **Figures**

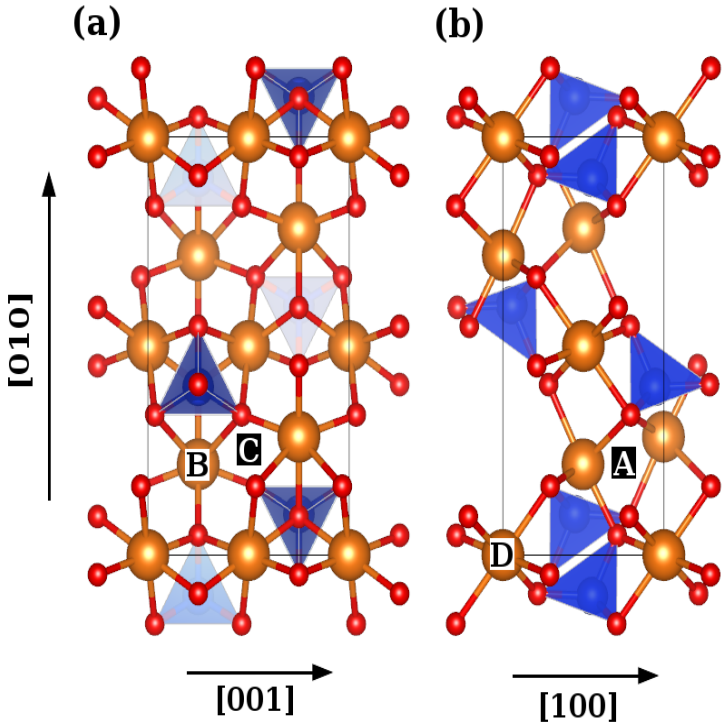

639

640 **Fig. 1** Olivine unit cell viewed down (a) the [100] cell direction, and (b) the [001] cell direction. Locations A, B,
641 C, and D are, respectively, the points in the unit cell through which the most stable core structures for the
642 [100](010) edge, [001](010) edge, [100] screw, and [001] screw dislocations pass. Visualization produced using
643 VESTA 3 (Momma and Izumi 2011).

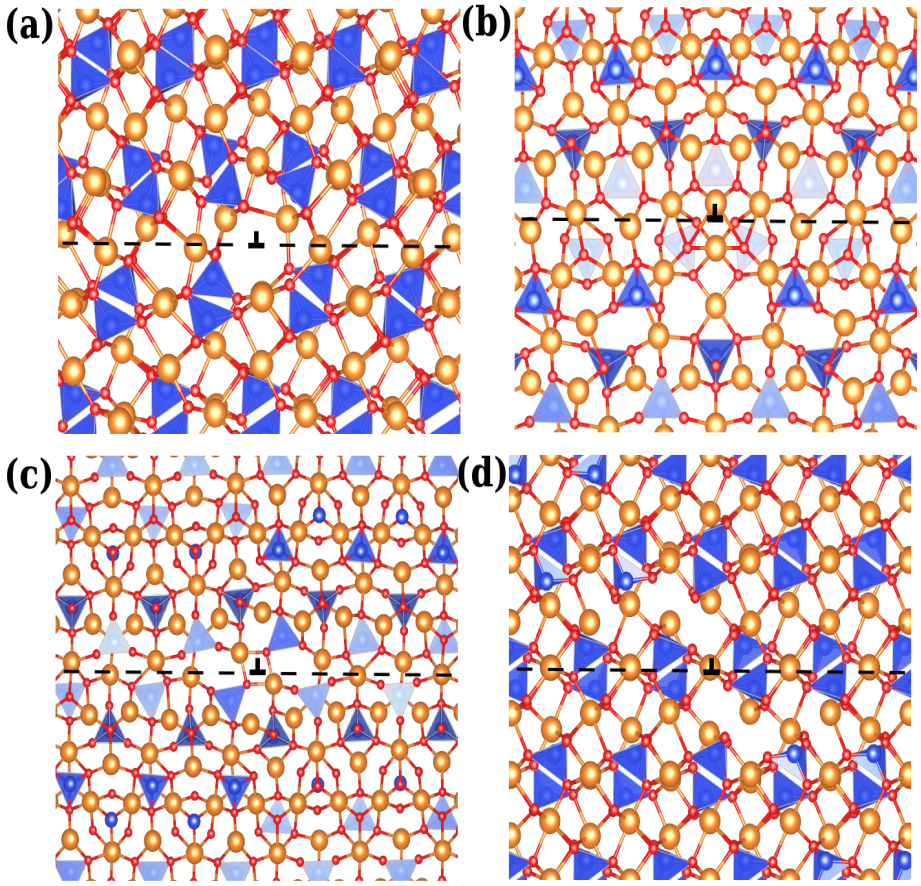

644

645 **Fig. 2** Atomic structures for the most stable core polymorphs of the (a) [100](010) and (b) [001](010) edge
646 dislocations, and (c) [100] and (d) [001] screw dislocations in forsterite. The dislocation line and (010) glide plane
647 have been marked. Visualization produced using VESTA 3 (Momma and Izumi 2011).

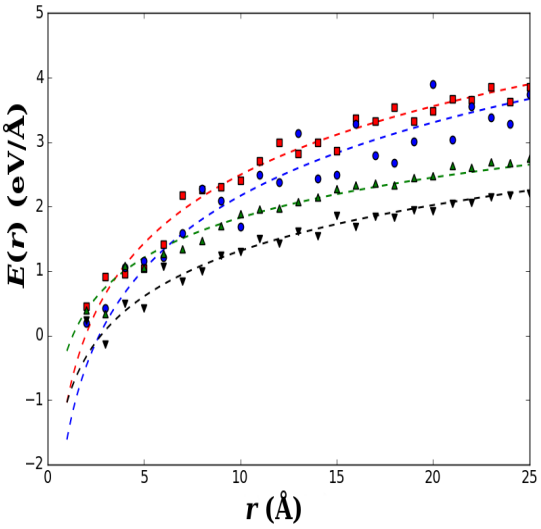

Fig. 3 Dislocation line energies as a function of distance *r* from the dislocation line, together with the energy curve fitted using equation (1). [100](010) edge, [001](010) edge, [100] screw, and [001] screw dislocations energies are shown using squares, circles, triangles, and inverted triangles, respectively.

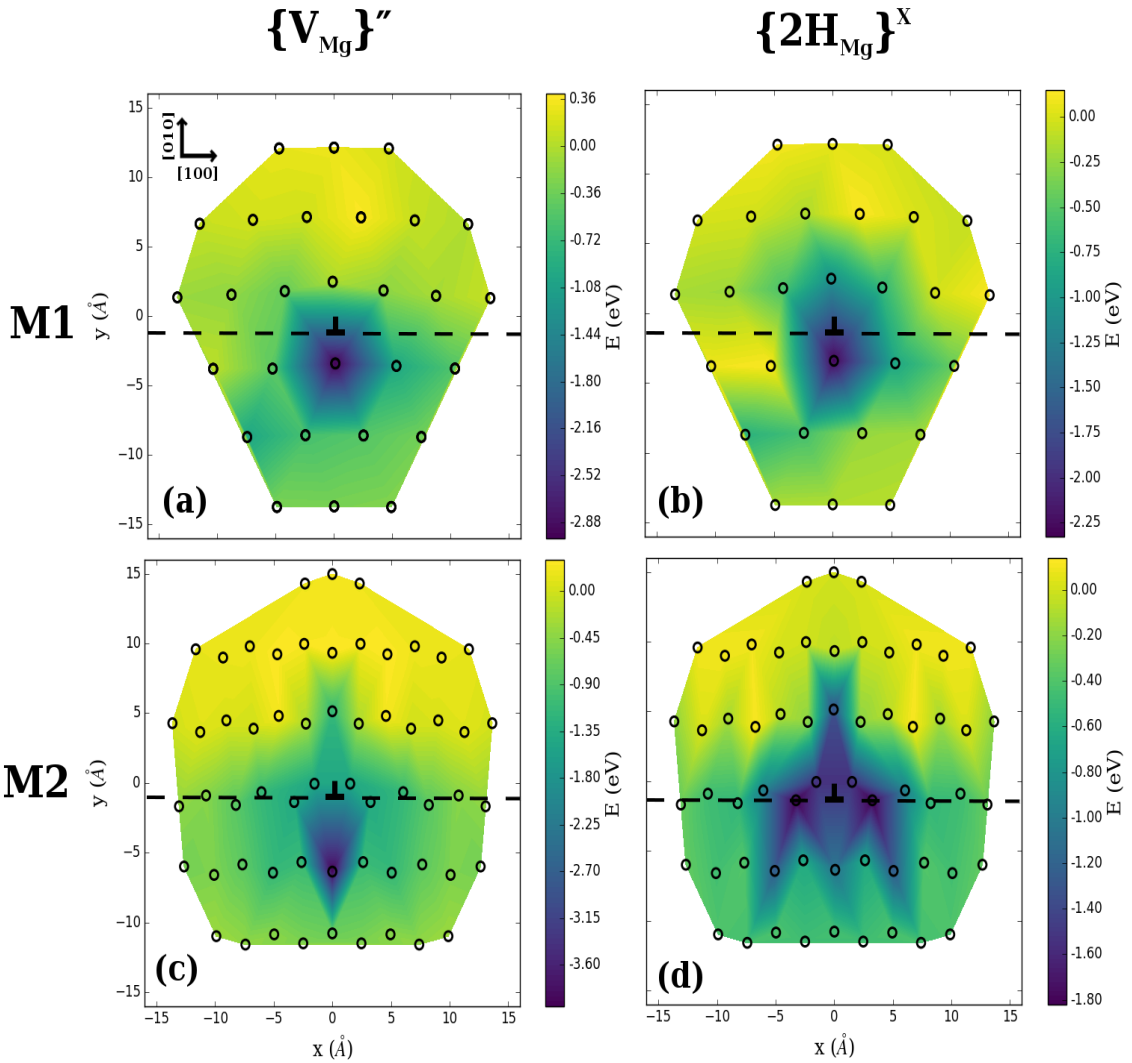

652

653 **Fig. 4** Segregation energies of bare and protonated Mg vacancies to the forsterite [100](010) edge dislocation. The
654 [001] lattice vector is normal to the image plane. Note that segregation energies for M2 defects are computed
655 relative to the corresponding defect in the bulk lattice, and are generally higher in energy than M1 defects. Both
656 the dislocation line and (010) glide plane are displayed.

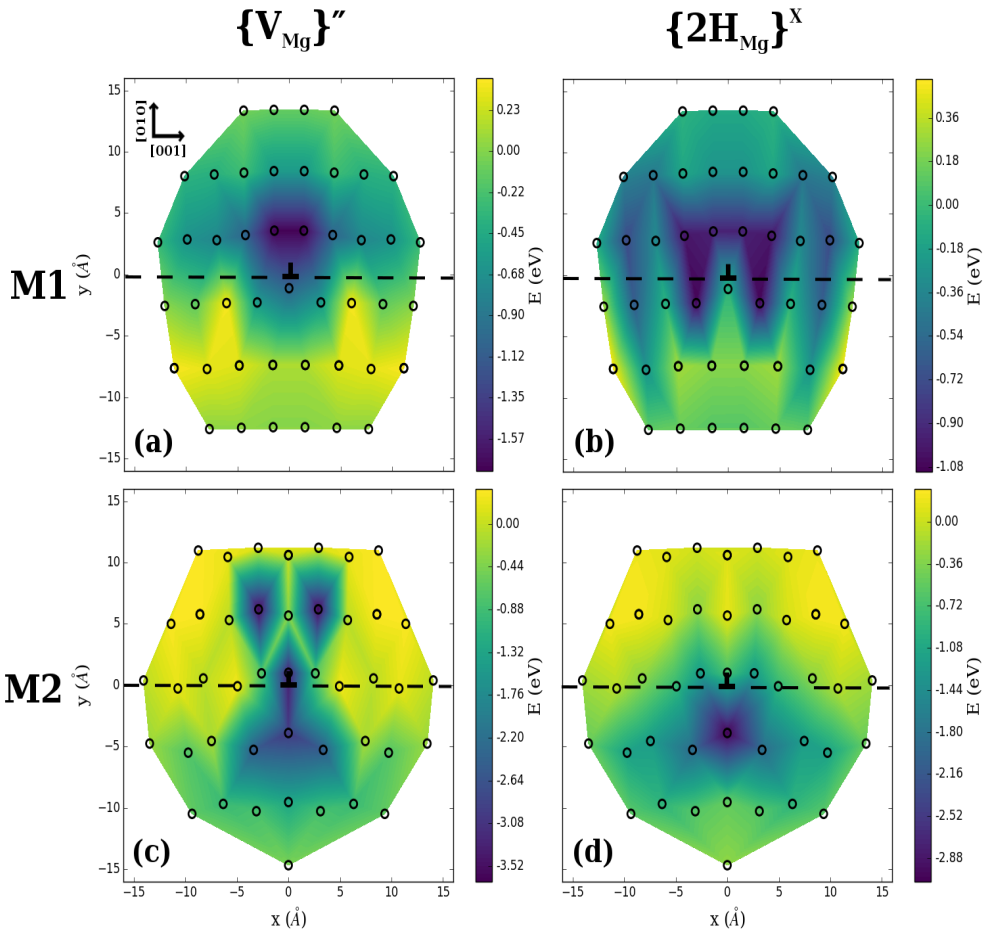

657

658 **Fig. 5** Segregation energies of bare and protonated Mg vacancies to the forsterite [001](010) edge dislocation. The
659 [100] lattice vector is normal to the image plane.

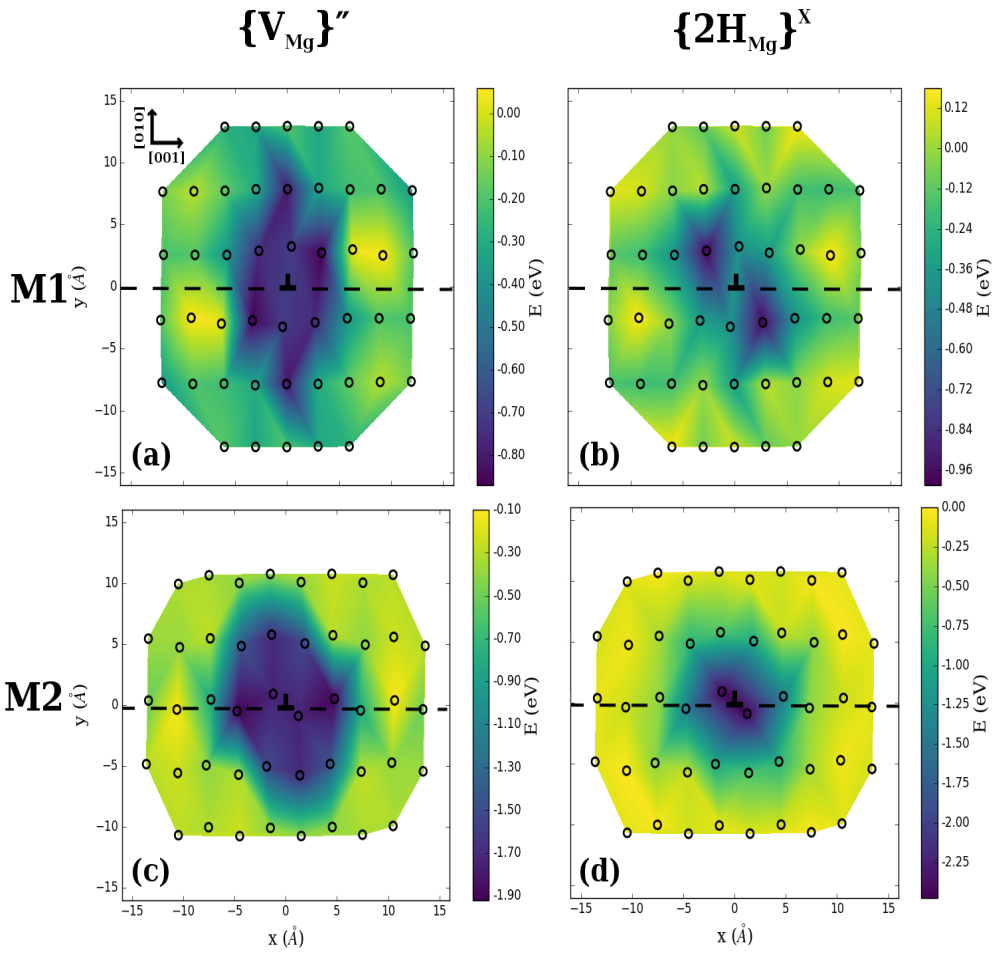

660

661 **Fig. 6** Segregation energies of bare and protonated Mg vacancies to the forsterite [100] screw dislocation. The
662 [100] lattice vector is normal to the image plane.

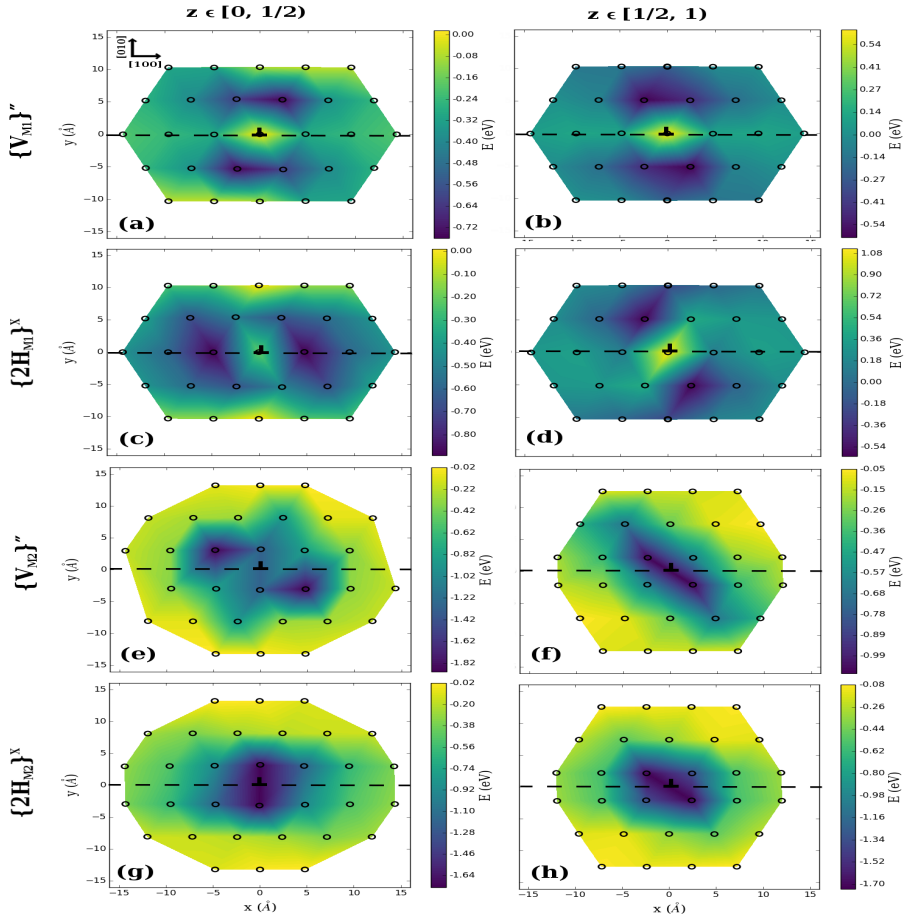

663

664 **Fig. 7** Segregation energies of Mg vacancies to atomic sites around [001] screw dislocations. To reflect the
665 modulated crystal structure of this dislocation along **x**, segregation energies for the "lower" (z ∈ [0, 0.5)) and
666 "upper" (z ∈ [0.5, 1.0)) regions are plotted separately.